THE JOURNAL OF PHYSICAL CHEMISTRY C
A JOURNAL OF THE AMERICAN CHEMICAL SOCIETY

pubs.acs.org/JPCC Article

Ion-Induced Surface Reactions and Deposition of Trimethyl(methylcyclopentadienyl)platinum(IV)

Mohammed K. Abdel-Rahman, Patrick M. Eckhert, and D. Howard Fairbrother*

Cite This: J. Phys. Chem. C 2022, 126, 15724−15735 Read Online

ACCESS | Metrics & More | Article Recommendations | Supporting Information

ABSTRACT: Ion-beam-induced deposition using $Me_3PtCpMe$ has been studied using a combination of ultrahigh vacuum (UHV) surface science studies performed on thin films and scanning electron microscopy (SEM) data of structures created under steady-state deposition conditions. X-ray photoelectron spectroscopy (XPS) data from monolayer thick films of $Me_3PtCpMe$ exposed to 1.2−4 keV Ar ions indicate that deposition is initiated by energy transfer from the incident ions to adsorbed precursor molecules leading to the loss of all four methyl groups and the likely decomposition of the Cp ring, yielding a deposit with a PtC_5 stoichiometry. This contrasts with focused electron-beam-induced processing (FEBIP), where deposition occurs as a result of electron excitation and the loss of only one Pt−CH_3 group. By comparing the rate of Pt(IV) reduction that accompanies either ion- or electron-induced decomposition of $Me_3PtCpMe$, it was determined that ion-induced deposition reaction cross sections are approximately two orders of magnitude greater. As a result of this higher reaction efficiency, ion irradiation was accompanied by some bimolecular methyl radical coupling to produce ethane. UHV studies also revealed that ion-induced deposition was followed by sputtering of Pt and C atoms at comparable rates. These fundamental insights provided by the UHV studies provided the basis to understand SEM data obtained on structures that formed under steady-state deposition conditions. In particular, the observation of "ring-like" deposits could be rationalized by sputtering in the center of the deposition region where the Ar^+ flux was sufficiently high to produce a precursor-limited regime, while deposition occurred in ion-limited regimes at the periphery of the deposition region where the Ar^+ flux was lower. These results demonstrate the utility of using data from a UHV surface science approach to better understand the composition and influence of reaction conditions on deposits formed during ion-beam-induced deposition of organometallic precursors.

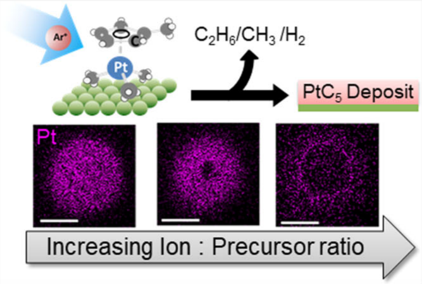

■ INTRODUCTION

Focused ion-beam-induced deposition (FIBID) and focused electron-beam-induced deposition (FEBID) are charged particle bottom-up nanofabrication techniques that directly fabricate 2D and 3D metal-containing nanostructures.[1−4] The use of charged particles grants precise control over beam position for nanoscale pattern writing without the use of a mask while simultaneously providing control over process-relevant factors like particle energy and flux. Moreover, these techniques do not require organic solvents and, as such, are more environmentally benign and less wasteful than traditional lithography, which typically requires spin coating of photoresists and solvent-based development steps. The inherent control that can be exerted over the growth conditions allows for regulation of the as-deposited properties, such as field strength in magnetic cobalt Hall sensors[5] and resistivity in gold contacts,[6] while the spatial precision inherent to charged particle deposition allows not only for the growth of standalone structures but also modification of previously produced objects as well. Growth of highly sharp carbon whiskers on silicon atomic force microscope (AFM) tips[7] and repair of lithographic masks[8] are among a variety of applications where these charged particle techniques have been applied.

In charged particle deposition techniques, volatile organometallic precursors, often those used in chemical vapor deposition (CVD), are injected into a vacuum chamber where they adsorb transiently onto a substrate surface. The adsorbed precursor is then subjected to a primary beam of high-energy (>500 eV) charged particles (ions or electrons), causing the precursor molecules to decompose in a spatially defined region of the substrate. The products of the dissociation are nonvolatile precursor fragments which form the deposit, along with volatile fragments which desorb and are pumped away.

One of the biggest issues with charged particle deposition techniques is the relatively poor metal content produced in the deposits compared to thermal deposition techniques such as CVD and atomic layer deposition (ALD). An illustrative example can be found in the behavior of one of the most

Received: July 25, 2022
Revised: September 1, 2022
Published: September 14, 2022

https://doi.org/10.1021/acs.jpcc.2c05255
J. Phys. Chem. C 2022, 126, 15724−15735

frequently studied precursors, $Me_3PtCpMe$, which works exceptionally well for CVD with a deposit purity of nearly 100%.[9] The elevated reaction temperatures and use of reactive gases like H_2 and O_2 allow for high purity. In contrast, the same precursor does not yield deposits with comparable purity when used as a FEBID/FIBID precursor. Thus, for FEBID, Pt purities are typically less than 20%.[10,11] In contrast, examples of FIBID deposits using He^+ and Ga^+ ion beams suggest higher purity can be achieved with C/Pt ratios of 4:1 or better, exceeding 20% Pt purity.[12,13] Indeed, the purity of deposits produced by FIBID is usually higher than FEBID, although ion implantation is observed with the use of Ga^+ ion beams,[14] leading to 5[15]−30[13]% gallium content. This can be mitigated using ions like He^+[12,16] or Ar^+, already commonly used in helium ion microscopes and focused ion-beam milling instruments, which have reduced ion implantation issues. However, compared to FEBID, another one of the drawbacks of FIBID is that, in common with other ion-beam-mediated deposition techniques, there is an innate competition between ion-induced deposition and ion-induced sputtering processes.[1,3,12,13]

To improve the composition and structure of deposits created from FIBID and FEBID, it is necessary to better understand the elementary reaction steps involved in the respective deposition processes. In this respect, previous surface science studies have investigated the electron stimulated reactions of adsorbed $Me_3PtCpMe$ molecules,[17,18] revealing that deposition of $Me_3PtCpMe$ in FEBID proceeds through the loss of a single methyl group under the influence of electron-beam irradiation, resulting in a C/Pt ratio of 8:1 under UHV conditions and in steady-state deposits.[18] Others have further shown that under high electron flux, this ratio can be reduced, although the ultimate Pt purity is still less than 17%.[19] In FEBID, it is also known that deposition is initiated by low-energy electrons inducing dissociation of adsorbed precursor molecules, primarily through either a dissociative electron attachment or dissociative ionization process.[19] In comparison, the fundamental bond-breaking processes involved in ion-induced deposition processes have only been studied for a small number of precursors.[1−4] One of the challenges is that ion-induced reactions are more complex as they can proceed via new pathways for precursor decomposition beyond secondary electron generation through mechanisms such as energy transfer by collision with adsorbed precursor molecules and localized thermal effects. Ar^+ ions have vastly more momentum (4.6×10^{-21} N·s at 1 keV) than electrons (1.7×10^{-23} N·s at 1 keV); therefore, there is a greater transfer of momentum to adsorbed precursor molecules, inducing bond cleavage upon collision. Moreover, sputtering effects are also important in FIBID processes. In the case of $Me_3PtCpMe$, the observation that the Pt content in FIBID[12,14] is higher compared to FEBID[18,19] suggests that different mechanistic pathways are involved. This provides a motivation to better understand the ion-induced reactions of $Me_3PtCpMe$ as a means to generate new knowledge that could inform the rational molecular design for new FIBID precursors.

In previous studies, we have shown significant differences in the effect of electron and ion irradiation on adsorbed organometallic precursor molecules. Thus, for $CpFe(CO)_2Re(CO)_5$[20] and $Fe(CO)_5$,[21] electron irradiation results initially in the loss of around 50% CO ligands, while further electron irradiation decomposes the residual CO, ultimately producing a film of metal oxides trapped in a graphitic matrix. In contrast, argon ion irradiation of the same adsorbed precursors causes complete molecular fragmentation and greater CO desorption through energy transfer to the adsorbed precursor molecules. The residual carbonaceous content in the films is then preferentially removed by ion sputtering, which under appropriate deposition conditions, can leave behind films with high metal contents. In the present study, Ar^+ ion-induced surface reactions of $Me_3PtCpMe$ adsorbed thin films were studied under UHV conditions *in situ* using X-ray photoelectron spectroscopy (XPS) to monitor the composition change of nonvolatile adsorbed species complemented by the identification and kinetic analysis of volatile species by mass spectrometry (MS). Experiments were also conducted to analyze the appearance and composition of deposits made under a constant partial pressure of $Me_3PtCpMe$ using scanning electron microscopy (SEM) and energy-dispersive X-ray spectroscopy (EDX). The effect of varying deposition conditions (e.g., Ar^+ ion-beam energies, ratio of Ar:$Me_3PtCpMe$ during deposition) on film composition was explored, and these results were rationalized by mechanistic inferences learned from the UHV surface science studies.

■ EXPERIMENTAL SECTION

UHV Studies. Studies designed to probe the fundamental molecular-level interactions of Ar^+ with adsorbed $Me_3PtCpMe$ precursor molecules were conducted in an ultrahigh vacuum (UHV) chamber (base pressure of $\sim 8 \times 10^{-9}$ Torr) equipped with capabilities for X-ray photoelectron spectroscopy (XPS) and mass spectrometry (MS).[20−23] Trimethyl(methylcyclopentadienyl)platinum(IV) ($Me_3PtCpMe$, 98%) was purchased from Sigma-Aldrich and transferred to a glass finger which was attached to a UHV compatible leak valve. The compound was purified by several freeze−pump−thaw cycles until impurities such as H_2O and O_2 were not detected with MS.

To generate an inert substrate, a 15×15 mm^2 piece of Ta (99.95%, Alfa Aesar) foil was intentionally oxidized to yield a thin film of mixed Ta oxides, herein referred to as TaOx. The presence of TaOx was confirmed with XPS by the presence of Ta 4f peaks with binding energies between 28 and 22 eV.[24,25] The Ta surface was oxidized by annealing the Ta foil at 500 K for 15 min in 1×10^{-6} Torr O_2.[26,27]

The TaOx substrate was cooled to 200 ± 5 K and exposed to 150 Langmuir (1.0×10^{-6} Torr × 150 s) of $Me_3PtCpMe$ to produce 1.9−2.1 nm films of $Me_3PtCpMe$. Film thickness was calculated from the attenuation of the Ta 4f envelope in the XP spectrum according to eq 1[28,29]

$$\ln\left(\frac{I}{I_0}\right) = -\frac{d}{\lambda \cos \theta} \tag{1}$$

where I and I_0 are the area under the Ta 4f envelope of the exposed and unexposed TaOx, respectively, λ (1.7 nm) is the inelastic mean free path of a Ta 4f photoelectron,[30] d is the film thickness in nm, and θ (54.7°) is the photoelectron takeoff angle relative to the hemispherical analyzer.

XPS was performed with a PHI 5400 using an Mg Kα X-ray source with an incident energy of 1253.6 eV and a pass energy of 22.38 eV unless otherwise stated. Photoelectron spectra were processed using CasaXPS, a commercially available software. The C/Pt ratios were normalized to the stoichiometric value of 9 for the $Me_3PtCpMe$ thin films prior to ion irradiation.

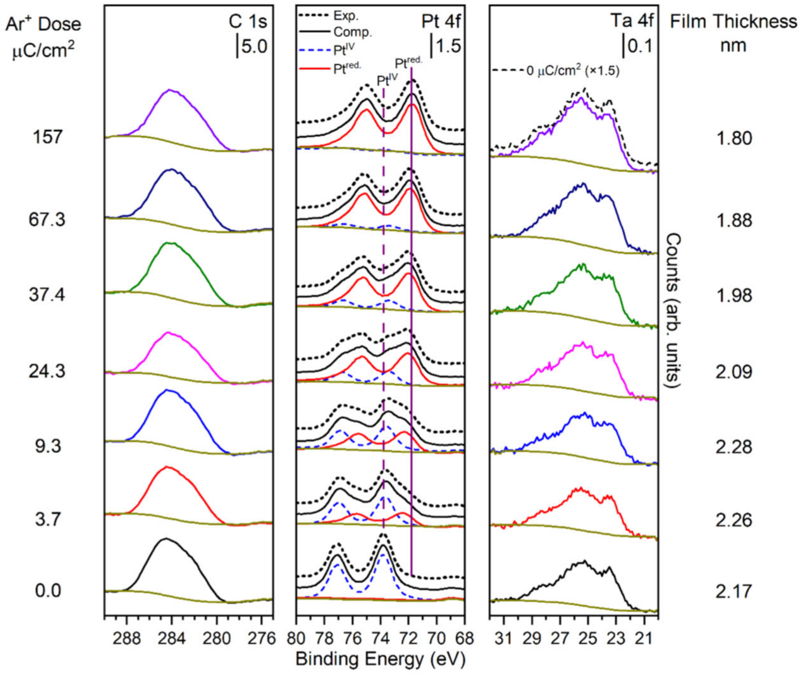

Figure 1. Evolution of C 1s, Pt 4f, and Ta 4f XP regions for a thin (≈2 nm) film of $Me_3PtCpMe$ on a cooled (200 ± 5 K) tantalum oxide substrate exposed to 1.2 kV Ar^+ ions at a flux of 1.1×10^{12} ions/s. In the Pt 4f region, the dashed blue line represents the Pt^{IV} component associated with the parent precursor molecules and the solid red line represents the reduced Pt species formed as a result of Ar^+ exposure. The binding energy of Pt^{IV} and $Pt^{red.}$ are indicated by the dashed and solid purple lines, respectively. The dotted line in the Ta 4f region represents the Ta signal at an Ar^+ dose of 0 $\mu C/cm^2$, which was amplified so as to be comparable with the Ta signal observed after an Ar^+ dose of 157 $\mu C/cm^2$. The C1s spectrum was acquired using an analyzer pass energy of 178.95 eV (to improve S/N), whereas the Pt/Ta 4f spectra were acquired in the same scan with an analyzer pass energy of 22.38 eV (to facilitate spectral deconvolution).

Mass spectrometry was performed with a Balzers Prisma QMA200 mass spectrometer. A PHI 04-303 differentially pumped ion gun served as the ion source for ion irradiation during experiments and sputter cleaning between experiments. Ion irradiation was conducted at 1.5×10^{-7} Torr to provide a target current of 180 nA corresponding to an ion flux of 1.1×10^{12} ions/s unless otherwise stated. In a more limited set of experiments, a Specs FG 15/40 flood gun was used as a source of electrons. The flood gun was used at an energy of 480 eV with a sample bias of +20 V to produce an incident electron energy of 500 eV. The target current was maintained at 20 μA during electron irradiation experiments.[18]

Deposits Created under Steady-State Conditions. Electron and ion-beam-induced deposits created from $Me_3PtCpMe$ under steady-state deposition conditions were prepared in separate chambers. Deposits were made on 20 × 20 mm^2 Si substrates purchased from Ted Pella, Inc. and introduced into the chambers through load-lock access doors. In each system, the precursor was introduced into the chambers using UHV-compatible leak valves with directional dosing lines to increase the local pressure of $Me_3PtCpMe$ near the silicon substrate. The ion-beam system (base pressure 5×10^{-9} Torr) was equipped with a PHI 04-303 differentially pumped ion gun and Stanford Research Systems RGA200 mass analyzer used to measure the gas phase ratio of $Me_3PtCpMe$ to Ar. Ion-beam-induced deposits were produced at room temperature with a constant Ar backing pressure of 5 mPa (measured with a PHI 11-065 ion gun controller at an emission current of 25 mA) and ion gun emission current of 5 mA over the course of 9 h with ion energies of 1.2 and 3.0 kV. The gas phase ratio of $Me_3PtCpMe$ to Ar was determined by the MS intensities of m/z = 15 and m/z = 40 amu, respectively.

The electron-beam system (base pressure 2×10^{-9} Torr) was equipped with a Kimball Physics ELG-2A electron gun with an EGPS-1022 power supply. Electron-induced deposits were made using electron energy of 2 keV with an emission current of 15 μA over 140 min with a $Me_3PtCpMe$ partial pressure of 2.0×10^{-6} Torr. In separate control experiments, we did not observe any increase in the substrate temperature during ion or electron-beam exposures, even when the ion or electron beam was incident upon a thermocouple attached to the backside of the sample holder. Consequently, our results are not influenced by thermal effects and can be attributed exclusively to the effects of low-energy ion−molecule and/or electron−molecule interactions.

A JEOL JSM-IT100 scanning electron microscope (SEM) equipped with an energy-dispersive X-ray spectroscopy (EDX) unit was used to image and analyze the elemental composition of the deposits.[23]

■ RESULTS

The XP spectra in Figure 1 display the C 1s, Pt 4f, and Ta 4f transitions of a 2 nm $Me_3PtCpMe$ film adsorbed at 200 K as a function of increasing Ar^+ dose (bottom to top). Previous studies have shown that under these conditions, $Me_3PtCpMe$ adsorbs molecularly in the absence of Ar^+ exposure.[18] With the onset of ion irradiation, the C 1s peak at 284 eV decreases in intensity, although the peak position remains unperturbed. Prior to Ar^+ exposure, the position of the Pt $4f_{5/2}$ and Pt $4f_{7/2}$ peaks were at 77.1 and 73.8 eV, respectively, and are attributed to Pt(IV) from the $Me_3PtCpMe$ precursor.[18,29] As a result of Ar^+ exposure, a new set of Pt $4f_{5/2}$ and Pt $4f_{7/2}$ peaks appear with values shifted toward lower (2.0 eV) binding energy

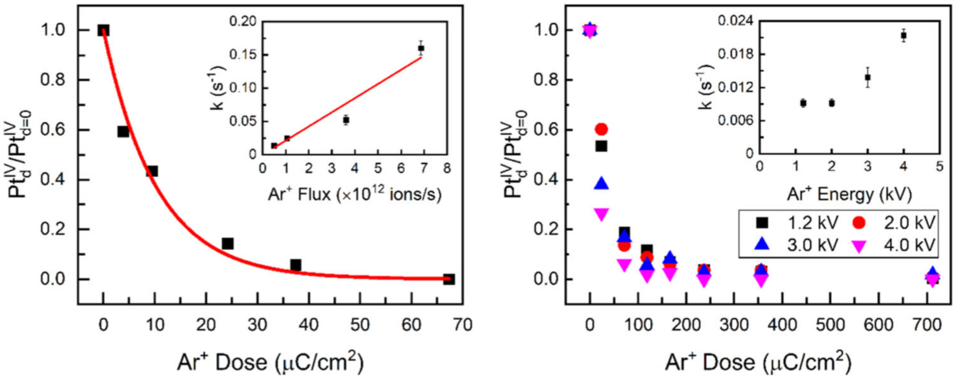

Figure 2. (Left) Decomposition (reduction) of the $Me_3PtCpMe$ precursor based on the decrease in the precursor (Pt^{IV}) coverage as a result of 3.0 kV Ar^+ bombardment (flux of 1.1×10^{12} ions/s)—solid red line represents the best fit based on a first-order kinetic process; inset highlights the dependence of the first-order rate constant on the Ar^+ flux. (Right) Rate of Pt(IV) reduction at varying Ar^+ beam energies at a constant Ar^+ flux of 1.1×10^{12} ions/s; inset highlights the dependence of the first-order rate constant on incident Ar^+ energy.

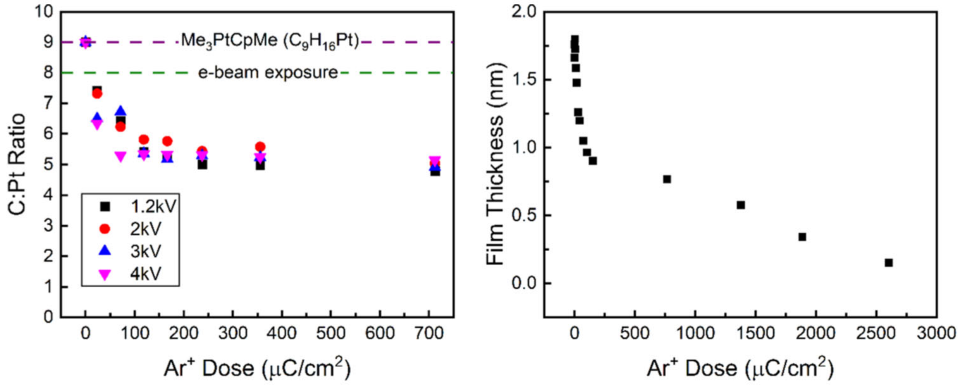

Figure 3. (Left) Change in the C/Pt ratio for $Me_3PtCpMe$ films as a function of Ar^+ dose measured at varying incident beam energies; the dotted purple and green lines show the C/Pt ratio observed for the initial $Me_3PtCpMe$ film and after exposure to 500 eV electrons (beam exposure of 36 mC/cm²), respectively. (Right) Change in film thickness with increased exposure to a 3 kV Ar^+ beam with a flux of 1.1×10^{12} ions/s.

compared to the parent peaks. This shift indicates Pt reduction from Pt(IV) to a reduced state. These two new Pt peaks increase in intensity with increasing Ar^+ dose, while the Pt(IV) peaks associated with the parent compound decrease in intensity. After an ion exposure of 157 μC/cm², only the new reduced form of Pt remains. Although the Pt peak position changes as a consequence of Ar^+ exposure, the Pt peak area remains constant during the Pt(IV) reduction indicating an absence of any measurable $Me_3PtCpMe$ sputtering. During Ar^+ exposure, Figure 1 shows that the intensity of the Ta peaks increases due to a reduction in effective film thickness; however, the Ta 4f peak shape remains relatively unchanged, indicating that the TaOx substrate does not undergo any ion-induced reactions.

Figure 2 compares the effects of ion flux (left) and incident ion energy (right) on the Pt reduction kinetics. The left panel of Figure 2 shows that at an ion energy of 3 kV and ion flux of 1.1×10^{12} ions/s, the Pt(IV) reduction is complete after an Ar^+ exposure of ≈70 μC/cm² and the rate of reduction can be well fit by a first-order process (solid red line). As a function of the ion flux, the Pt reduction can consistently be fit with a first-order kinetic process and exhibits a rate constant proportional to the ion flux (inset in the left panel of Figure 2). The rate of Pt(IV) reduction can also be followed as a function of ion-beam energy (Figure 2 right panel) at a constant ion flux. The rate constant remains roughly constant between 1.2 and 2 keV but increases as the ion energy increases from 3 to 4 keV (inset in the right panel of Figure 2).

In Figure 3, the left-hand panel shows the evolution of the C/Pt ratio as a function of ion dose. Regardless of the ion-beam flux or energy, the C/Pt ratio initially (ion doses <≈ 70 μC/cm²) decreases rapidly from the initial stoichiometric value of 9:1 ($C_9H_{16}Pt$) to 5:1, corresponding to a loss of ≈4 C atoms per Pt atom in the film. This rapid rate of change in the C/Pt ratio closely mirrors the Pt(IV) reduction rate (compare Figure 3 left and Figure 2 right-hand panels). For ion doses >≈70 μC/cm², however, the C/Pt ratio remains relatively unchanged. The green dotted line in the left-hand panel of Figure 3 shows that when $Me_3PtCpMe$ films are exposed to electrons (36 mC/cm² at 500 eV) rather than ions, the resulting C/Pt ratio decreases from 9:1 to only 8:1, consistent with previous results.[18] The right panel of Figure 3 shows the dependence of the film thickness on the Ar^+ dose. During the Ar^+ dose that corresponds to the Pt(IV) reduction (<≈70 μC/cm²), the film's effective thickness decreases significantly by 50%, corresponding to the change in the C/Pt ratio from 9:1 to 5:1. For ion doses >≈70 μC/cm², the film thickness decreases more slowly and with an approximately linear dependence on the ion dose.

The neutral volatile species produced when $Me_3PtCpMe$ films are bombarded by Ar^+ ions (Figure 4) were identified using MS. Prior to Ar^+ exposure, the bottom (black) spectrum in the left panel reveals the presence of UHV background gases

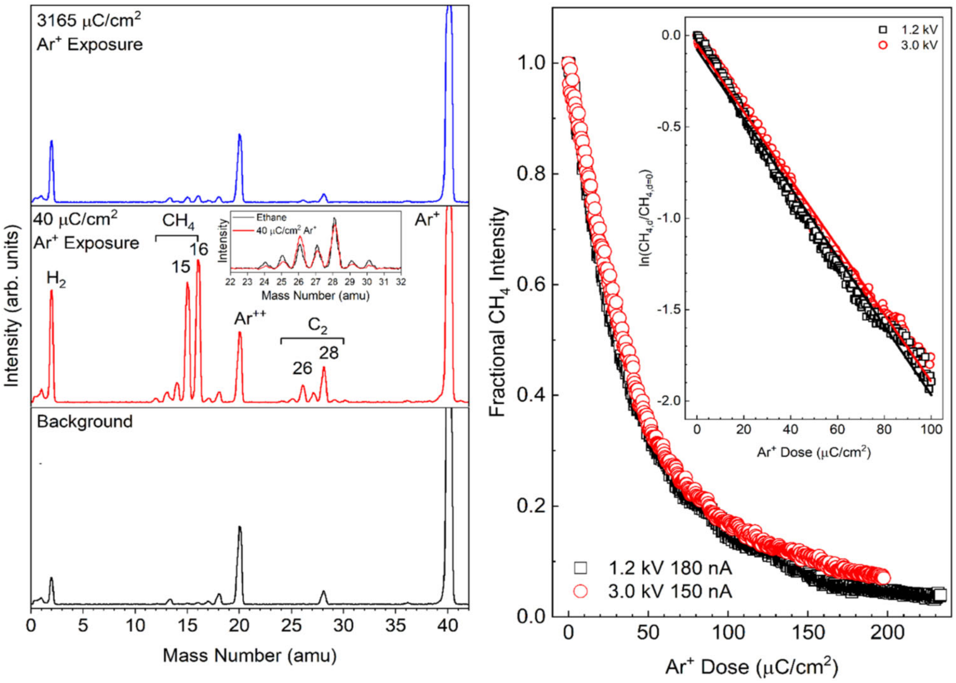

Figure 4. (Left) Mass spectra of the neutral desorption products observed during the ion-beam irradiation of $Me_3PtCpMe$. The film was irradiated with a 3.0 kV Ar^+ beam at a flux of 7.3×10^{12} ions/s. The bottom panel indicates the gas composition of the UHV chamber with 1.5×10^{-7} Torr Ar present prior to ion irradiation (the features at $m/z = 40$ and $m/z = 20$ correspond to Ar^+ and Ar^{++} ions formed by electron impact ionization of neutral Ar in the QMS). The middle panel displays the mass spectrum observed during the $Me_3PtCpMe$ film's exposure to 40 $\mu C/cm^2$ Ar^+, corresponding to an acquisition time of 15 s. The top panel displays the gas phase observed after 3165 $\mu C/cm^2$ (~1200 s) Ar^+ exposure. The inset in the middle panel compares the C_2 species observed between $m/z = 22-32$ with gas phase ethane. (Right) Kinetic profile for CH_4 production observed at $m/z = 15$ amu (right) for two different incident ion-beam energies. The inset shows the linearization of the kinetic decay profiles with the corresponding fits for a first-order decay process.

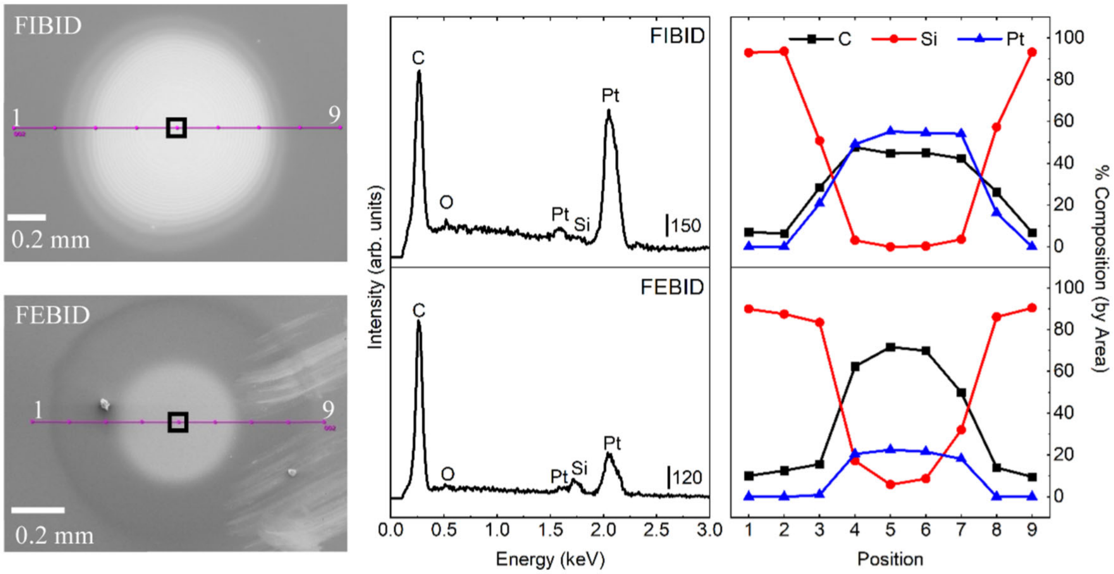

Figure 5. Comparison of Pt deposits made from FIBID (top row) and FEBID (bottom row) of $Me_3PtCpMe$. The Ar ion-beam-induced deposition was conducted at a constant total pressure of 3×10^{-6} Torr for 9 h at a beam energy of 1200 eV while maintaining a $Me_3PtCpMe/Ar$ ratio of 2:1 as determined by the ratio of $m/z = 15$ to $m/z = 40$ in the mass spectrum (see Figure S4). The electron-beam-induced deposition was conducted at a precursor pressure of 6×10^{-7} Torr for 140 min with a beam energy of 1000 eV. (Left-hand column) SED images of the FIBID and FEBID deposits; (center column) EDS of the FIBID and FEBID deposits, each taken at the center of the respective deposits. The peak intensities were calculated from Gaussian fits of the data against an asymmetric least squares baseline to correct for Bremsstrahlung radiation (see Figure S3). (Right-hand column) Elemental composition at various points across the deposits determined from EDS data. The SEM images and EDS spectra were all collected with a primary electron-beam energy of 5 kV.

(H_2, H_2O, and CO) and Ar ($m/z = 20(Ar^{2+})$, 40 amu(Ar^+)). The middle (red) spectrum in the left panel was acquired during the initial (40 $\mu C/cm^2$) exposure of the $Me_3PtCpMe$ film to Ar^+ at 3.0 kV corresponding to 15 s acquisition time of

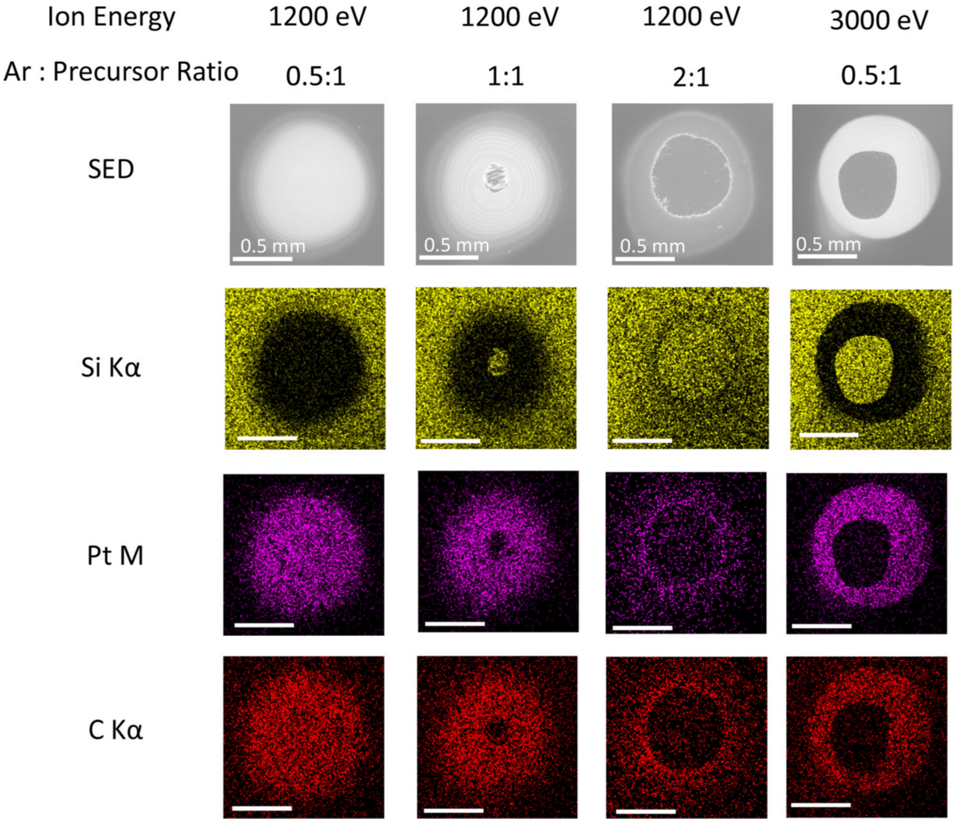

Figure 6. Elemental distribution maps of Si, Pt, and C highlighting the effect of deposition conditions on deposits created by ion-beam irradiation in the presence of $Me_3PtCpMe$. These depositions were created by maintaining constant partial pressures of Ar and precursor for 9 h. The precursor pressure varied between different depositions while the Ar pressure was held constant. The Ar/precursor ratio was determined by the ratio of $m/z = 40$ to $m/z = 15$ in the mass spectrum, respectively (see Figure S4). The SEM images and elemental distribution maps obtained from EDS were collected with a primary electron-beam energy of 5 kV.

the QMS. New peaks are observed at m/z = 15, 16, 24−27, and 29−30 amu, along with noticeable increases in existing peaks at 2 and 28 amu. In the inset to the middle panel, the MS from 24 to 30 amu was compared with the spectrum for ethane (99.99%); the latter was acquired separately at a pressure of 1.0×10^{-6} Torr. Contributions from background gases were subtracted from both spectra. The overlay of the two spectra reveals a qualitatively similar fragmentation pattern between m/z = 24−30 for gas phase ethane and the C2 species observed during Ar^+ bombardment of the $Me_3PtCpMe$ film. The top (blue) spectrum in the left-hand panel of Figure 4 was acquired after an ion exposure of 3165 $\mu C/cm^2$ at a sufficiently high ion dose where the new peaks observed during Ar^+ irradiation have returned to nearly background levels. The right panel of Figure 4 compares the rate of CH_4 production (measured at m/z = 15 amu) for different beam energies and ion fluxes (black: 1.2 kV, 1.1×10^{12} ions/s; red: 3.0 kV, 9.4×10^{11} ions/s). When the methane production is plotted in terms of the ion dose for both beam energies, both CH_4 profiles follow the first-order decay with similar rate constants; this first-order dependence is supported by the linear relationship in the inset and noting the invariance of the half-life for CH_4 decay (30 $\mu C/cm^2$) on the $Me_3PtCpMe$ coverage (see Figure S1), the latter measured by the film thickness.

Steady-state deposits formed on Si substrates using ion-beam and electron-beam deposition in the presence of constant partial pressure of $Me_3PtCpMe$ and with the substrate at room temperature are compared in Figure 5. In the SED images, the bright area corresponds to areas with higher Pt content. The Pt distribution is greater in the FIBID deposit due to the larger spot size of the ion beam. The EDX spectra for the deposits are presented in the middle column, while the elemental composition determined from EDX data at various points across the deposits is shown in the right-hand column.

Elemental distribution maps of the C K, Si K, and Pt M X-ray lines for FIBID deposits created under different deposition conditions are presented in Figure 6. The first three columns show deposits created using an ion-beam energy of 1200 eV but under different gas phase conditions. With a 0.5:1 Ar/precursor ratio, a uniform deposit is observed within the deposition region. As the ratio of ions to precursor molecules increases to a 1:1 Ar/precursor ratio, however, there is evidence of localized sputtering in the center of the deposit observed by the greater intensity of the Si K and the absence of Pt M and C K X-rays. At an even higher Ar/precursor ratio of 2:1, the highest concentration of Pt in the deposit is found in a "ring" structure at the periphery of the deposit. The right column corresponds to a deposit created at 3000 eV with a 0.5:1 Ar/precursor ratio. This deposit has Pt and C concentrated within the irradiated area; however, there is significant sputtering at the center of the deposit, as evidenced by the presence of Si in the EDX maps.

■ DISCUSSION

UHV Surface Science. Upon exposure to Ar^+, XPS and MS data support the idea that all of the $Pt-CH_3$ and $C-CH_3$

bonds in the adsorbed $Me_3PtCpMe$ dissociate, creating volatile C1 and C2 carbon species in the form of methyl radicals and ethane and leaving behind a deposit with a PtC_5 stoichiometry. Previous studies have shown that methyl radicals ejected during the dissociation of $Me_3PtCpMe$ abstract hydrogen from the walls of the UHV chamber are detected by the QMS as methane.[18,31] Thus, the overall ion-beam-induced decomposition of adsorbed $Me_3PtCpMe$ can be summarized by eq 2 below

$$\begin{aligned}&Me_3Pt^{IV}CpMe\ (ads)\\ &\xrightarrow{Ar^+} C_5Pt^0\ (s) + {}^\bullet CH_3(g)/CH_4(g) + C_2H_6(g)\end{aligned} \tag{2}$$

During this Ar^+ ion-beam dissociation step, XPS analysis of the Pt(4f) region reveals that $Me_3Pt^{IV}CpMe$ undergoes reduction (Figure 1), although the Pt coverage does not decrease, indicating that the physisorbed $Me_3PtCpMe$ is not subject to ion-induced sputtering. This is consistent with the absence of any mass fragments uniquely identified with $Me_3PtCpMe$ (e.g., mass 54 and 79)[18] during ion-beam irradiation (data not shown). In contrast to Pt(4f), the C(1s) intensity decreases with increased Ar^+ exposure indicating a loss of carbon as gaseous hydrocarbons. The C(1s) peak shape remains unperturbed, indicating that tantalum carbide, which would appear at 282 eV, is not formed during FIBID of $Me_3PtCpMe$. To identify the Pt oxidation state associated with the new species formed during ion irradiation, the XP spectrum of $Pt^{II}(CO)_2Br_2$ was compared to the initial and final spectra from $Me_3Pt^{IV}CpMe$. The Pt $4f_{7/2}$ peak of $Pt^{II}(CO)_2Br_2$ appears at 73.3 eV, in agreement with reported values for Pt^{II} nanoparticles created from $PtCl_2$.[32] In contrast, the Pt $4f_{7/2}$ peak in the PtC_5 matrix is observed at 71.8 eV, significantly lower than expected values for a Pt^{II} species and closer to the binding energy of metallic Pt at 71.1 eV.[33,34] Consequently, on the basis of the Pt $4f_{7/2}$ binding energy measured for the fully reduced Pt species being measured at 71.8 eV in Figure 1, we identify these new Pt species as Pt^0 atoms embedded in a graphitic matrix.

As expected on the basis of eq 2, the rate of Pt^{IV} reduction and CH_3 desorption follow first-order kinetics as a function of ion dose (exposure time) under conditions of constant ion flux and ion energy. Figure 2 shows that the rate constant for Pt^{IV} reduction and CH_3 desorption is proportional to the ion flux at a constant ion energy (see Figure 2). Indeed, a constant half-life of ≈10 $\mu C/cm^2$ was determined for Pt reduction across a range of ion fluxes (see Figure S2), consistent with the idea that the reaction is first order with respect to ion flux. In terms of ion energy, Figure 4 shows the rate of methane production for two $Me_3PtCpMe$ films of comparable thickness exposed to different Ar^+ energies (1.2 and 3 kV) but similar ion fluxes, 1.1×10^{12} and 9.4×10^{11} ions/s, respectively. Figure 4 shows that the decay profiles are nearly identical with reaction cross sections of $(8.0 \pm 0.1) \times 10^{-15}$ and $(7.1 \pm 0.2) \times 10^{-15}$ cm^2, respectively. This supports the conclusion that the ion-induced decomposition of adsorbed $Me_3Pt^{IV}CpMe$ molecules is largely independent of the incident ion energy. However, using the rate of Pt^{IV} reduction as a metric, the reaction rate is observed to increase for energies in excess of 3 kV.

The reaction kinetics with respect to the precursor coverage can be determined on the basis of the relationship between the half-life for methane production and the initial Pt film thickness. Thus, half-lives of 29 and 26 $\mu C/cm^2$ were determined for initial film thicknesses of 1.53 and 0.88 nm, respectively (see Figure S1). This observation of a half-life for methane production, which is independent of precursor coverage, is consistent with the first-order reaction kinetics that has been used to model the Pt(IV) reduction process; thus, the rate of reaction can be expressed by eq 3.

$$\frac{[Me_3PtCpMe]_d}{[Me_3PtCpMe]_0} = e^{-\sigma d} \tag{3}$$

where σ is the total reaction cross section in cm^2 and d is the ion dose in $\mu C/cm^2$.

The total reaction cross section (σ) can be calculated from the dependence of the cross section on the ion flux (see Figure 2 left panel inset), as reported previously,[18] using eq 4, where σ is the reaction cross section in cm^2, k is the first-order rate constant in s^{-1}, I is the ion flux in ions/s, and A is the ion-irradiated (sample) area in cm^2.

$$\sigma = \frac{k}{I} \times A \tag{4}$$

Using this approach, the reaction cross section for FIBID of $Me_3PtCpMe$ with Ar^+ is determined to be $(1.23 \pm 0.04) \times 10^{-14}$ and $(7.97 \pm 0.03) \times 10^{-15}$ cm^2 from the XPS and MS analyses, respectively. These values are approximately two orders of magnitude larger than the cross-section values ($\approx 1 \times 10^{-16}$ cm^2) previously reported for FEBID of $Me_3PtCpMe$.[18]

In terms of the reaction mechanism, we believe that the Pt−CH_3 and C−CH_3 bond cleavage can be explained by an impulsive energy transfer that occurs from incident Ar^+ to adsorbed $Me_3PtCpMe$ precursor molecules. Our experimental observations that the reaction kinetics are proportional to the precursor coverage and the ion flux support the idea that reactions occur as a consequence of interactions between individual Ar^+ and adsorbed precursor molecules. Based on a simple kinematic energy transfer model, the average energy transferred from the incident ions to the precursor molecules will be well in excess of the bond dissociation energies (BDEs) for the various bonds present.[35] Under these circumstances, our previous studies have shown that bonds with the lowest BDE are broken preferentially at the highest rates.[21] In this respect, the BDE for Pt−CH_3 (1.7 eV)[36] is significantly lower than the other BDEs in $Me_3PtCpMe$; therefore, Pt−CH_3 bond cleavage is the favored dissociation pathway, leading to methyl radical production. The next bond dissociated would likely be the Cp−CH_3 bond, which has an estimated BDE of 2.7 eV based on a difference of approximately 0.4 eV between reported values for aromatic C−H and C−CH_3 bonds in various methylarene compounds.[37] In contrast, the high BDE of C−C bonds in ferrocene (≈5 eV)[21,38] and the Pt−Cp bond (3.25 eV)[39] compared to the C−H bonds (3.1 eV for Cp−H and 3.9 eV for Me−H)[37] mean that ion-induced reactions with the cyclopentadienyl ring are dominated by C−H bond cleavage and the formation of a carbonaceous matrix, along with hydrogen desorption, the latter observed by an increase in m/z = 2 during ion bombardment (Figure 4). Although H_2 production is also observed in Figure 4, it is difficult to quantify because of residual H_2 in the UHV chamber. The production of CH_3 radicals is also supported by the observation of ethane, which can reasonably be assumed to occur via a methyl radical coupling reaction with a near-zero activation energy.[40] We determined a ratio of 3:1 for the production of methane to ethane by comparing the intensities of m/z = 15 and 26 in Figure 4 to those of fixed pressures of

Scheme 1. Ion-Induced Deposition of $Me_3PtCpMe$ under Steady-State Conditions

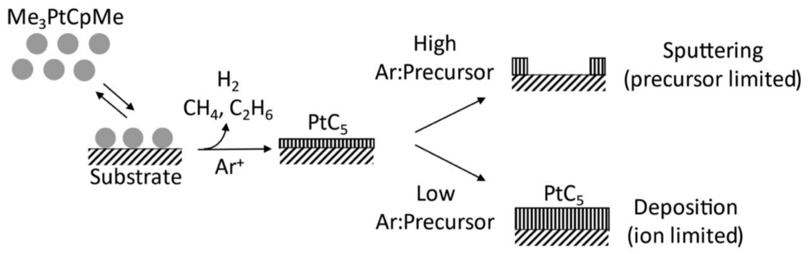

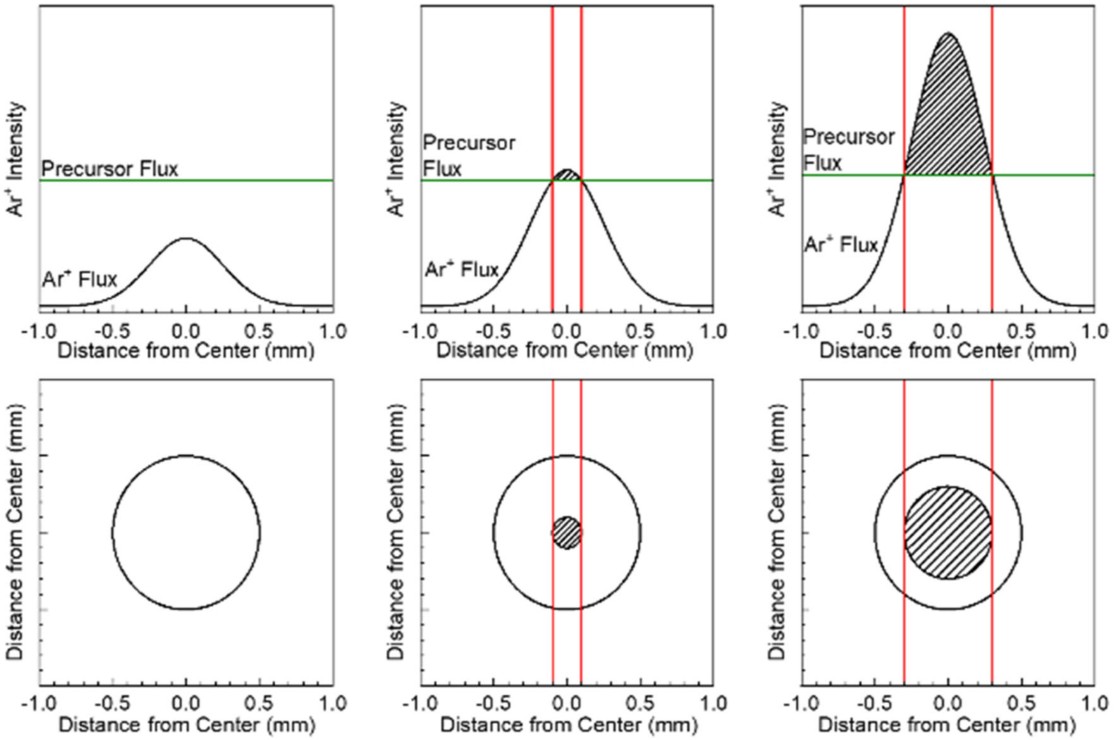

Figure 7. (Top) Schematic representation of the Ar^+ and precursor flux within the deposition region at (left) 0.5:1, (center) 1:1, and (right) 2:1 Ar^+/precursor ratios. (Bottom) A simulated deposit resulting from (left) 0.5:1, (center) 1:1, and (right) 2:1 Ar^+/precursor ratios. Sputtering (shaded region) occurs when the ion flux reaches a precursor-defined threshold (green line) and is spatially confined to the area circumscribed by the red lines.

pure methane and ethane, respectively (Figure S3). In summary, we conclude that the Ar^+-induced deposition of Pt from $Me_3PtCpMe$ results in the desorption of four methyl radicals, approximately 25% of which undergo bimolecular coupling to generate ethane, leaving behind those carbon atoms associated with the Cp ring to form a PtC_5 deposit. Changes in the effective film thickness during ion-beam irradiation are also suggestive of platinum coalescence and nucleation. Thus, Figure 3 shows that during precursor decomposition described by eq 2, there is a reduction in effective film thickness of 50%, although all of the Pt atoms and > 50% of the nascent carbon atoms are retained in the deposit. This implies that precursor decomposition is accompanied by densification and/or nucleation within the remaining atoms. As the film is exposed to ion doses in excess of 70 $\mu C/cm^2$, the film composition remains constant while the thickness decreases (Figure 3). This behavior is attributed to ion-induced sputtering of the residual PtC_5 film.

Results from the present study can also be compared with analogous FEBID studies of $Me_3PtCpMe$, where dissociation has been shown in the gas phase and surface science studies to be a consequence of dissociative electron attachment (DEA), leading to the loss of a single Pt−CH_3 group.[18,19,31] The DEA process occurs when a molecule acquires a low-energy electron to form a transient negative ion (TNI). The TNI then dissociates into vibrationally excited anionic and neutral radical species.[19,23,41] In the case of $Me_3PtCpMe$, the TNI $[Me_3PtCpMe]^-$ dissociates into $[Me_2PtCpMe]^-$ and $^{\bullet}CH_3$. As a consequence, in FEBID, when Pt^{IV} reduction is complete, the resulting species has PtC_8 stoichiometry,[18] whereas in the present study, FIBID occurs as a result of impulsive energy transfer from the ion to the adsorbate, leading to the loss of all CH_3 species and the formation of a PtC_5 species (Figures 2 and 3). In previous electron irradiation studies of $Me_3PtCpMe$ conducted under UHV conditions, no ethane or other C2 hydrocarbons were detected.[18,31] In ion-beam interactions with $Me_3PtCpMe$, however, the greater reaction cross sections coupled with the greater degree of Pt−CH_3 bond cleavage produce significantly higher fluxes of methyl radicals, favoring bimolecular coupling reactions to form ethane. In broader terms, the results of this study are consistent with other recent studies of charged particle interactions with organometallic precursors where ion and electron-beam reactions proceed by different mechanisms. Specifically, electron-induced dissociation of organometallic precursors proceeds via electronic excitation, while ion-beam dissociation is initiated by energy transfer from the incident ion to the adsorbate.[20−22]

Deposits Formed under Steady-State Conditions. Pt deposits formed under steady-state FIBID and FEBID conditions (constant partial pressure of $Me_3PtCpMe$ and Ar ion flux) were compared in terms of composition and morphology with SEM and EDX. The ion-beam-induced deposit (Figure 5, top row) produced a structure approximately 1 mm wide. Line profile analysis indicates the deposit has sufficient thickness to impede Si Kα X-ray detection across the center of the deposit, accounting for the invariant Pt concentration in the center of the deposit. In contrast, the electron-beam deposit (Figure 5, bottom row) resulted in a 1 mm wide deposit with a 0.5 mm wide region in the center where the deposit is thick enough to obscure any Si signal. For structures formed from both FIBID and FEBID, the Pt:C ratio is uniform within the deposit.

Based on the UHV surface science data, we can propose Scheme 1 for the ion-beam deposition of $Me_3PtCpMe$ under steady-state conditions:

The structures formed by FIBID under different deposition conditions (Figure 6) can be understood by first considering the fate of PtC_5 deposits formed by the ion-induced decomposition of the $Me_3PtCpMe$ precursor, as described in Scheme 1. In the limit of excess precursor molecules (the ion-limited regime), the decomposition of precursor molecules to form involatile PtC_5 is accompanied predominantly by additional adsorption and ion-induced decomposition of $Me_3PtCpMe$. These conditions provide for sustained film growth. As the relative concentration of Ar^+ to precursor increases, however, the deposition process enters the precursor-limited regime, and deposition of any PtC_5 species is now followed predominantly by Ar^+ bombardment rather than further precursor adsorption. Under these circumstances, sputtering becomes the dominant process.

In addition to the fate of the deposited atoms, the other important consideration is the spatial variation in the flux of precursor molecules and ions within the deposition region (Figure 7). In our experiments, the precursor flux is held roughly constant between different experiments and can be assumed to be relatively uniform within the deposition region, the latter defined by the overlap between the flux of precursor molecules and ions on the substrate. In contrast, the ion flux is expected to exhibit a roughly Gaussian intensity profile consistent with our own independent analysis of the beam's profile, determined by imaging the beam profile on a fluorescent target.

The left-hand column in Figure 7 describes conditions where the flux of ions is low enough at all points within the deposition region so that deposition occurs is in an ion-limited regime. Under these conditions, a uniform deposit is created whose shape and thickness are determined by the Gaussian ion-beam profile. This situation corresponds to the deposits observed in the left-hand column of Figure 6, where the Ar^+/precursor ratio is 0.5:1. The central column of Figure 7 describes the situation where the ion intensity has increased to the point where the ion flux in the very center of the deposition region is now high enough to cause sputtering to dominate over deposition (precursor-limited). This explains why in Figure 6, as the Ar^+/precursor ratio increases to 1:1, a "hole" appears in the center of the deposition region. As the ion intensity increases further to an Ar^+/precursor ratio of 2:1, the area within the deposition region where sputtering dominates over deposition increases and consequently the size of the "hole" increases as well. This scenario is illustrated by the right-hand column in Figure 7.

To explore the effect of ion energy, a deposit was created at an ion energy of 3 kV with a 0.5:1 Ar^+/precursor ratio and compared to its 1.2 kV counterpart (Figure 6). The resulting deposit shows a large central crater where sputtering is dominant; whereas, at 1.2 kV, there is no evidence of any sputtering. In separate studies, we investigated the effect of ion energy on the sputter rate of PtC films (Figure S5) using XPS and determined sputter rates of 45 ± 1 and 32 ± 1 pm/min at ion energies of 3 kV and 1.2 kV, respectively, with a constant ion flux. Thus, under the same Ar^+/precursor ratio, deposition at Ar^+ energy of 3 kV will lead to more sputtering compared to 1.2 kV, particularly in the central regions of the deposit where the ion flux is highest. This difference in the balance between deposition and sputtering rationalizes the difference in Figure 6 for the deposits created under the same Ar^+/precursor ratio but at different ion-beam energies.

EDX Composition Analysis. The use of energy-dispersive X-ray spectroscopy (EDX) is ubiquitous in material analysis as it quickly provides compositional information. However, deposits created by charged particle deposition techniques present a significant challenge for reliable EDX analysis. The most significant complication is a direct result of the precursors used for metal deposition, which typically contain a high Z metal, e.g., Au, W, Rh, Pt, along with low-Z ligands, e.g., C, O, or F. Quantification of light, low-Z elements by EDX is difficult, given that their only X-ray lines are below 1 kV.[42] Consequently, X-rays emitted by light elements can suffer from significant absorption within the material itself, as well as the window of the detector which can absorb these low-energy X-rays. In the case of C, spurious signal intensity can also arise with the use of carbon-based detector windows from which X-rays may be produced or if contamination and dead layers are present on the X-ray detector, the latter being particularly prevalent for cryogenic EDX detectors.[42] The sensitivity of carbon analysis is further exacerbated by samples with significant surface roughness where low-energy X-rays are preferentially attenuated, leading to anomalous calculated composition.[43,44]

While these issues alone can hinder light element analysis, the addition of high Z elements serves to further complicate matters. Thus, heavy elements like Au and Pt form dense solids with high electron and X-ray attenuations, leading to increased error from X-ray self-absorption. Moreover, they produce higher-energy X-rays with greater photon yields than light elements, which contributes to increased error from X-ray fluorescence, e.g., excitation of C-Kα by Pt-Mα photons. While the matrix-induced error is typically corrected automatically using ZAF models, which correct for X-ray detection based on atomic number (Z), X-ray self-absorption (A), and X-ray fluorescence (F), the exact methods of correction may be hidden behind proprietary vendor software and even when done manually may not be able to correct for the magnitude of absorption and fluorescence in a light/heavy binary system. Although more advanced corrections exist, namely $\varphi(\rho z)$ methods that correct for the depth distribution of characteristic X-rays, which depends on the mass density (ρ) of the analyte and depth (z) at which the X-rays are produced, they require standards.[42] In the case of Pt/C, standards are problematic as they are primarily organometallic compounds, which are usually volatile, almost invariably electron-beam sensitive, and have high C/Pt ratio. Standards should ideally represent a similar matrix as the material of interest to appropriately account for ZAF factors, so typical low-density organometallic compounds would be a poor match for dense metallic deposits. Elemental standards are not ideal for Pt/C materials either because of the significant difference in X-ray and electron interactions between elemental C, Pt, and compounds containing both elements.

Another issue can arise from electron-beam-induced deposition of carbon onto a sample during analysis,[45] whose rate of formation is highly variable (e.g., measurements taken before or after instrument maintenance, cleanliness of samples and sample holders, etc.). Because almost any X-rays produced by surface carbon will escape the surface, a contaminant layer of only a few nanometers may add spurious additional C Kα intensity to the EDX.

Beyond issues associated with X-ray analysis itself, the Pt/C system presents further inherent difficulties. Thus, Pt (and some other Pt group metals) have an often-unreported N-line doublet near 250 eV.[46] While the relative intensity of this N-line is low, for a material with a high Pt:C ratio, the overlap with the C-Kα X-ray at 277 eV cannot be ignored.[47] Further complicating this region is an escape peak artifact near 300 eV caused by Pt M-line X-rays exciting Si-Kα X-ray emission in the EDX detector itself. As the Pt concentration in deposited materials increases, the contribution of these overlapping peaks will serve to further reduce the accuracy of C analysis. For these reasons, the use of EDX in the analysis of charged particle-induced Pt/C deposits should be viewed qualitatively.

Although a quantitative determination of deposit composition using EDX is challenging and fraught with difficulty, EDX data have values as a means of qualitatively comparing samples analyzed under the same operating conditions using the same instrument. In this respect, it is evident from Figure 5 that the Pt content in structures created by FIBID are significantly higher than in FEBID, consistent with the expectations of the UHV surface science studies. Under steady-state deposition conditions in FIBID, the surface is bombarded by ions in the presence of constant partial pressure of precursor molecules. Although the formation of silicon carbide is not observed in deposits (Figure 6), silicon carbide may have been sputtered away during the deposition process. Cross-sectional EDS is best suited for determining the deposit/substrate interface, which is the subject of a future study. In addition to ion−molecule collisions, the interaction of the ion beam with the surface will also generate secondary electrons that could themselves initiate deposition as in FEBID. However, if deposits generated by FIBID are formed by secondary electron interactions with adsorbed precursor molecules, we would expect that the film's composition would mirror FEBID, inconsistent with our experimental observations. Consequently, the significantly higher Pt content observed in FIBID supports the postulate that the deposition of $Me_3PtCpMe$ occurs as a result of ion−molecule interactions rather than reactions between the adsorbate and low-energy secondary electrons generated by the interactions of the primary ion beam with the substrate.

■ CONCLUSIONS

Low-energy (<5 keV) argon ion irradiation of $Me_3PtCpMe$ thin films leads to energy transfer between the incident ions and adsorbed precursor molecules. This leads to the reduction of the Pt(IV) atoms, causes the four CH_3 groups to desorb, and triggers the decomposition of the Cp ring, resulting in a film of Pt atoms embedded in a carbonaceous matrix with PtC_5 stoichiometry. Further ion irradiation results in physical sputtering of the deposited Pt and C atoms at similar rates. This contrasts with electron-induced reactions of $Me_3PtCpMe$, which are characterized by electronic excitation of the precursor and the loss of a single CH_3 group by means of dissociative electron attachment. A comparison of Pt reduction rates reveals that compared to electron-induced deposition, the ion-induced deposition cross sections are two orders of magnitude greater. These findings provided the basis to understand the structures formed by ion-induced deposition under steady-state conditions. Specifically, under conditions where the precursor:ion ratio was sufficiently high within the deposition region, uniform deposits were observed whose thicknesses were determined by the rate of deposition, the latter controlled by the Ar^+ flux. In contrast, as the ion flux increased, "ring-like" deposits were observed. This phenomenon is rationalized by the prevalence of sputtering in the center of the deposit where the Ar^+ flux is sufficiently high to sputter any deposited Pt and C, whereas deposition occurred at the periphery of the deposit where the Ar^+ flux was lower. In summary, this study illustrates how data obtained from UHV surface science studies can be used to provide molecular-level information that can help rationalize both the composition and structure of deposits formed by ion-beam-induced deposition of organometallic precursors.

■ ASSOCIATED CONTENT

Supporting Information

The Supporting Information is available free of charge at https://pubs.acs.org/doi/10.1021/acs.jpcc.2c05255.

> Kinetic trace of CH_3 fragments (m/z = 15) for $Me_3PtCpMe$ films of different thicknesses; kinetic decay profile of the Pt^{IV} XPS component at varying ion flux; independently acquired mass spectra of methane, ethane, and the ion-induced reaction products of $Me_3PtCpMe$; and mass spectra of the reaction mixture during steady-state FIBID of $Me_3PtCpMe$ at different reactant ratios with SEM images of resulting deposits (PDF)

■ AUTHOR INFORMATION

Corresponding Author

D. Howard Fairbrother − *Department of Chemistry, Johns Hopkins University, Baltimore, Maryland 21218-2685, United States;* orcid.org/0000-0003-4405-9728; Email: howardf@jhu.edu

Authors

Mohammed K. Abdel-Rahman − *Department of Chemistry, Johns Hopkins University, Baltimore, Maryland 21218-2685, United States;* orcid.org/0000-0002-8028-5258

Patrick M. Eckhert − *Department of Chemistry, Johns Hopkins University, Baltimore, Maryland 21218-2685, United States;* orcid.org/0000-0001-6520-1821

Complete contact information is available at: